

Comparison of Blind Imaging Performance of Fizeau and Michelson Type Arrays for a Partially Resolved Object

Casper van der Avoort^{a,b}, Jan-Willem den Herder^b and Joseph Braat^a

^aDelft University of Technology, Lorentzweg 1, 2628 CJ Delft, The Netherlands;

^bSpace Research Organisation of the Netherlands, Sorbonnelaan 2,
3584 CA Utrecht, The Netherlands

ABSTRACT

This paper compares two well-known types of interferometer arrays for optical aperture synthesis. An analytical model for both types describes the expected output, in terms of photon counts. The goal is to characterize the performance of both types of array for blind imaging of a wide-field or extended object that would be partially resolved by a single elementary aperture. The spectrum of the source is assumed to be constant over the source and in time, but broad-banded. The light levels are such that only a few photons per pixel or bin are received. The simulated interferometer responses are discussed. The process of reconstructing the source from the ‘recorded’ responses is presented, but not discussed in this paper. It turns out that both types of interferometer are capable of imaging a partially resolved source with high spatial frequencies present all over the source.

Keywords: Interferometry, homothetic mapping, wide-field imaging, aperture synthesis

1. INTRODUCTION

In the work presented here, we try to compare the blind imaging capabilities of two different types of telescope arrays for aperture synthesis imaging. ESAs *Darwin* mission¹⁴ has as goal to characterize planets around nearby stars. The technique applied for this goal is nulling interferometry. Since that requires an array of optical telescopes in space, the mission could be valuably extended by an imaging component.¹⁷ High resolution images can be made with a technique called *aperture synthesis*, where the light collected by the separated telescopes is jointly detected and processed.¹ Several beam combination schemes exist, that all have their strong and weak points. In this paper we model two of these beam combination schemes, together with the data processing they require, since a combination of hardware design and data analysis method will lead to optimal performance for the specific goal of imaging an extended scene.¹⁶ In the end of the modeling, both numerical models can produce realistic shot-noise limited detection signals per array configuration. Moreover, the forward model can be inverted in a regularized and noise suppressing way, so that an estimate can be made of the extended ‘image’ that produced these detected data.

Special attention goes to the performance at low light levels. The two modeled arrays (having an equal number and size of telescopes and throughput efficiency) receive an equal number of photons – while stable coherent integration is assumed to a degree less strict than the nulling task requires – and the methods of combination and detection determine then how and where these photons with Poisson count statistics end in the detected data. After presentation of the two types of beam combination and detection in Section 2, the nature of the detected signals will be discussed in Section 3 and the results for low light levels will be shown. Discussion follows in Section 4 and conclusions are drawn in Section 5.

Further author information: (Send correspondence to Casper van der Avoort)
E-mail: c.vanderavoort@tnw.tudelft.nl, Telephone: +31 15 2789407

2. TYPES OF ARRAYS

To start with, special attention should be drawn to the confusing labeling of interferometers in literature. Often, arrays are simply classified as being ‘Michelson-type’ or ‘Fizeau-type’. To be able to address and discuss all features of each interferometer correctly, the following distinctions are made.

- **Wavefront Collection.** In many European papers, the distinction between Fizeau and Michelson-types relates to the method of wavefront collection. The method to collect and relay parts of the wavefronts emitted by the stellar object distinguishes between Fizeau and Michelson. Respectively, the wavefronts are *relayed curved or flat*. Fizeau and Stephan (around 1890) used an aperture mask in front of the primary collector of a telescope. Hence, from the beginning of the ‘transport’ of the partial wavefronts to the point of combination, the wavefronts are curved. An interferometer with separated collection elements should therefore have *curved primaries* with the radius of curvature corresponding to the synthetic aperture in which they are positioned, to be called an array of Fizeau-type.

The experiments by Michelson and Pease (Mt. Wilson, around 1900) took place by collecting parts of the same wavefront and transporting them – while still collimated – to the beam combiner, being a regular telescope, *not* a beamsplitter. Although the wavefronts were collected by flat mirrors, there is no essential difference with separated telescopes outputting a collimated beam. For a mirror (or siderostat) the beam compression or magnification is $M = 1$, while a telescope as collector can be configured to produce any beam compression ratio. Collecting and transporting *flat* partial wavefronts is essentially the Michelson-type. Nearly all optical long-baseline interferometers are of this type.

- **Beam Combination.** Traditionally, the possibilities are pupil-plane combination or image-plane combination and are often mentioned as Michelson* or Fizeau-mode. In all cases the energy in the beams will be focused onto one or more detectors. The combination of the beams can be *before focussing or co-axial or in focus or multi-axial*. When combined co-axially, a beamsplitter is used to combine two beams pairwise, of which possibly one or both beams was already the combination of two others. The co-axially combined beam will then be focused onto one or more detectors for intensity readout. Combining in a non-co-axial way means that the focusing optics needed to focus all energy in the beams onto (one or) more detectors should be as large as the total area in which the (compressed) beams are placed and will therefore be larger than a single beam diameter. The beams can simply be placed at a fixed distance side-by-side (e.g. Michelson experiment, densified pupil imaging) or have a general magnification, position and orientation (general non-homothesis, see⁶). A special case is *homothesis*, when the orientations and relative positions of the beams at the entrance pupil are exactly copied and scaled so that before focusing, the partial wavefronts are arranged as an exactly scaled copy of the partial wavefronts before the primary collectors (e.g. the Large Binocular Telescope, earth imaging Multi-Aperture Optical Telescopes).
- **Fringe Encoding.** The options for fringe encoding are temporal or spatial encoding or a combination of both. These options are coupled to method of collection or method of combination. Operating a masked aperture (Fizeau collection) will result in spatial fringes in focus. Co-axial combination will need temporal encoding (varying the pathlength difference of a beam pair) to produce interference fringes. For general non-homothetic, non-co-axial combination, fringes for a part of the field-of-view will be spatially encoded and the full field-of-view can be covered by adding temporal encoding. Generally, interferometric imaging provides high resolution images for regions of the field-of-view in which fringes (encoded in some way) can be observed.
- **Detection.** The signal from which an image is to be reconstructed is a summation of electrical fields (partial wavefronts) focused together. This optical signal can only be measured as intensity. The method of fringe encoding makes that this intensity in focus varies with position (spatial encoding) or with time (more precisely with changing pathlength differences between pairs of beams, realized by a time dependent modulation signal). To obtain all encoded information, the detection should be able to measure this time

*Here, the ‘Michelson’-label refers to the famous Michelson–Morley experiment, in which beams were combined co-axially.

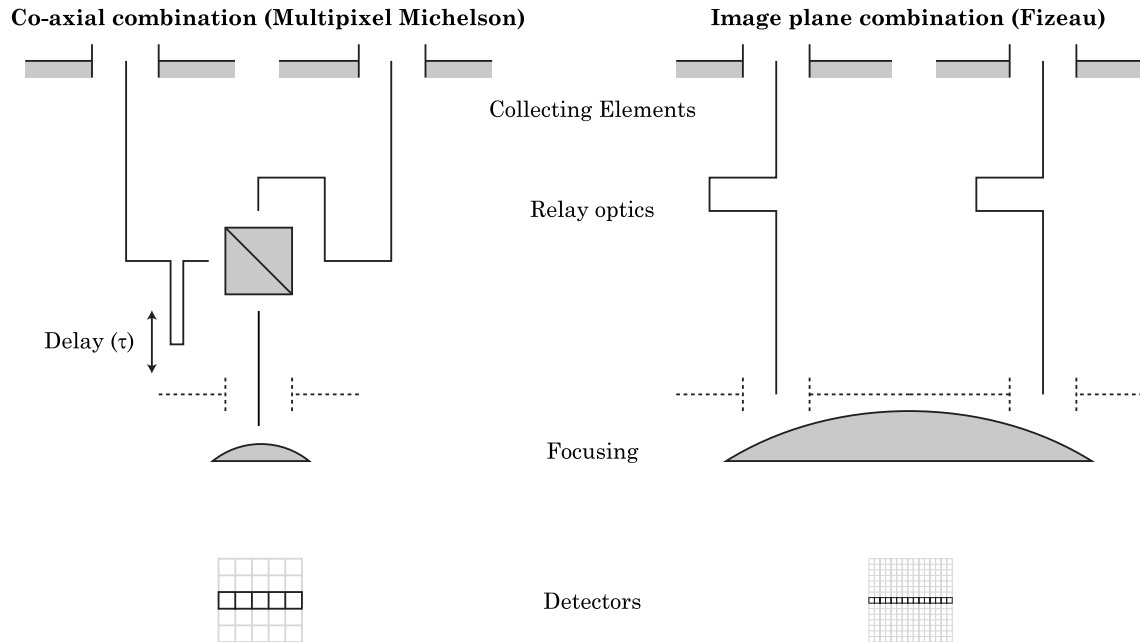


Figure 1. Two types of beam combination for optical aperture synthesis: co-axial combination for ‘Multipixel Michelson’ and image plane combination ‘Fizeau’. The necessary number of pixels in the detector is indicated schematically.

and place dependent intensity. The detector should consist of enough and small enough elements to sample the spatially varying intensity (where the spatial frequency is principally determined by the combination method and can possibly vary with array dimensions) and the detector should be able to collect multiple intensity sets when temporal encoding is applicable. Additional restrictions for the dimension of each detection element lie in the size of a single collector and – as mentioned – in the separation distance of collectors. The overall dimension of the detector should (angularly) cover the desired field-of-view. The elements can be either photosensitive devices or fibers, feeding the local electric field to an intensity detector elsewhere. The detector can consist of one, a few, or many detection elements and will produce one or a few readouts per array configuration.

When designing an optical interferometer for certain stellar observations, the subject or class of objects to be observed determines the desirable basic lay-out of the interferometer array. The methods of collecting and combining the partial wavefronts poses constraints on the hardware of the array, e.g. coatings and materials for optics and the noise characteristics of the detector. The data analysis is rather determined by the method of fringe encoding and the detector. It should be clear that both domains of hardware and software counterpose restrictions on each other. This may limit compatibility of available software with desirable hardware for example, but it should also be clear that hybrid combination and detection schemes are possible so that new ways of detection and postprocessing arise.

In this study, only the two classical beam combination schemes are chosen. Co-axial combination is most common² whereas the homothetic combination type¹⁰ is often referred to as the only one being capable of covering a wide field-of-view. In spite of the clarified terminology, we shall address the two modeled arrays as ‘Multipixel Michelson’ and ‘Fizeau’, whereas the latter should have been labeled ‘homothetic Michelson’ according to the definitions. The collection and combination schemes are depicted in Fig. 1 for the case that there is no beam compression.

To illustrate the principles used here in the simulation and analysis more easily, only a two-element interferometer is considered. This means that the high angular resolution is only attained in one direction. Therefore, all simulations are one dimensional. The detector is a line-detector; the source is a *linear* luminosity distribution

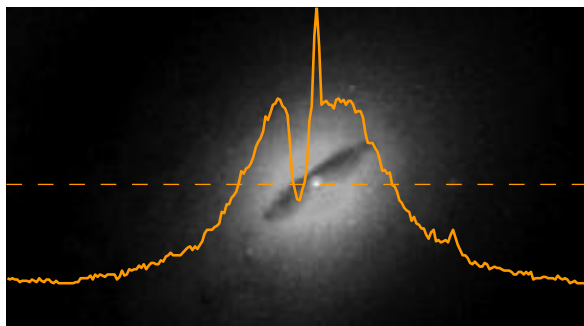


Figure 2. The young galaxy UGC00597 (Hubble Space Telescope image). The dashed line indicates the position of the slice of the image of which the pixel values were used as linear luminosity distribution $L(\alpha)$. The thick line represents this function. The angular dimension of this source was set to be twice the diffraction limited spot size of a single telescope.

on the sky. The source that we use as an example in the simulation is depicted in Fig. 2. This is the young galaxy UGC00597, as observed by Hubble Space Telescope. We chose the dimensions of our object to be ~ 2 PSFs and the detector array to be ~ 3 PSFs. The dish diameter and PSF size are specified further. The cross-section in the figure indicates the linear luminosity function that is actually used in the simulation. The PSF size is indicated and the narrowest feature in the source is about 1/8th of this diameter. The number of resolution elements in the simulated source is 231, which are not necessarily resolvable by the synthetic aperture. Other specifications of the simulation parameters for both arrays are listed in Table 1. The divisions by 8 indicate that a fringe is sampled in respectively 8 delay bins or 8 detector pixels.

Table 1: Measurement settings for simulations

Case	Pixels	Pixel Size	OPD Range	OPD Stepsize
Multiple Detector Michelson	6 (3 PSFs)	$\simeq \text{PSF}/2$	$2B_{\max}\alpha_{\max}$	$\lambda_c/8$
Fizeau	256 (3 PSFs)	$\text{PSF} \frac{D}{B_{\max}}/8$	–	–

The nulling requirements for the Darwin mission provide a co-phased array with all metrology necessary to fulfill image overlap and fringe stability to a degree that is far more strict than needed for imaging. Therefore, we assume no fringe shifts in this simulation and diffraction limited PSFs for all beams. Given the Darwin hardware, a number of interesting targets for imaging has been acquired. This led to the imaging requirements listed in table 2.

Table 2: Darwin imaging requirements

Requirement	Specifications
Flux	1 μJy per hour
Bandwidth	4 ... 28 μm
Field-of-View	3 arcsec (= 14.5 μrad)
Resolution	1 mas (= 4.9 nrad)
Dynamic range	1 : 100
Spectral Resolution	200 bands
1 Jy (Jansky) = $10^{-26} \text{Wm}^{-2} \text{Hz}^{-1}$	

The complete wavelength range will be covered in a few channels, typically half octaves. For the simulation, we take $\lambda = 6 \dots 10$ microns. This range has no astrophysical reason and the spectrum is a Gaussian envelope.

The spectral aspects of the imaging requirements lie outside the scope of this article, that just demonstrates the imaging process. In the current design, the telescope primaries have a diameter $D = 3.5$ meter. This yields a PSF with an angular diameter on the sky of $d_{\text{Airy}} = 2.44\lambda_c/D = 7\mu\text{rad}$.

To model the detector response of such a source for the co-axial type, the ‘traditional’ fringe prediction according to the quasi-monochromatic theory of partial coherence³ as applicable to radio interferometry could not be used. This theory assumes a narrow bandwidth, a resolved stellar object and point-like collecting elements. These assumptions are not applicable to our goal of observation. Therefore, a linear convolution model was developed. For homothetic imagers like LBT, imaging by joint deconvolution already was the existing approach.¹³

3. INTERFEROMETER RESPONSE

Image deblurring and tomography (or image reconstruction) are both well-studied inverse problems. The inverse problem of deblurring has been treated in the domain of optical astronomy, even with space variant convolution kernels, as in the case where images from the Hubble Space Telescope were improved¹¹ or for image reconstruction with a homothetic array by joint deconvolution of multiple snapshots.¹³ The tomography approach (image construction from other data than a degraded version of that image) is most resembled by radio imaging techniques⁸ where fringe visibilities are related to the source brightness function. When only treating complex visibilities, the limited extent of the *convolution kernel* (both in finite coherence length as well as limited spatial extent of the PSF) is not taken into account in the way that wide-field optical interferometry requires. Therefore, a field-variant, multi-dimensional convolution kernel should be implemented in the convolution model for co-axial imaging.

The paper on algorithms for LBT image reconstruction¹³ compares some linear and iterative algorithms to each other. Maximum Entropy and CLEAN are two very popular, but missing algorithms in that paper. It is stated that both algorithms perform only better in the case of point-like objects or scenes that are mainly black except for a few pixels. For our example of recovering a wide-field extended source with unknown distribution or discontinuities, we choose the most simple linear inverse method. It is known that iterative or non-linear approaches will perform better in retrieving sharp edges of the object⁹ but the non-linear approaches are not as easy to implement as linear methods. We want to demonstrate the inversion of the wide-field fringe data in a linear and simple way, knowing that the results will probably be better with a complicated non-linear algorithm.

In this section, the described fringe responses at all pixels for various baseline lengths are taken as ‘measured’ data to put into a linear system of equations that is inverted by applying Tikhonov regularisation, a very popular linear method.

3.1. Definition of forward and inverse problem — Co-Axial

The luminosity distribution on the sky (the stellar object) $L(\alpha)$ is a positive function of the angular coordinate α . On the detector plane, in-focus, this will produce a recordable intensity $I(\alpha, \tau)$ that will change with the applied pathlength difference τ in units of meters. We know that

$$I(\alpha, \tau) = \sum_i R_i(\alpha, \tau), \quad (1)$$

where R is a baseline dependent point source *response function*, measured in intensity and i is a running integer corresponding to all possible point source locations, in this case one per evenly spaced synthetic resolution element. Essentially, R is the product of an envelope function (PSF) scaled by the normalized fringe intensity pattern. This allows us to write $R(\alpha, \tau)$ according to

$$R(\alpha, \tau) = L(\alpha_0) \int_{k_{\min}}^{k_{\max}} \left| \frac{2J_1[\pi k D(\alpha - \alpha_0)]}{[\pi k D(\alpha - \alpha_0)]} \right|^2 w_\lambda [1 + \cos[\pi k(\tau - \tau_0)]] . \quad (2)$$

Here, J_1 is the first-order Bessel function, $\tau_0 = B_k \sin(\alpha_0) \approx B_k \cdot \alpha_0$ and k indicates a wave number, not to be confused with the subscript of B_k . The cross-section is an unaberrated Airy function and the integrated

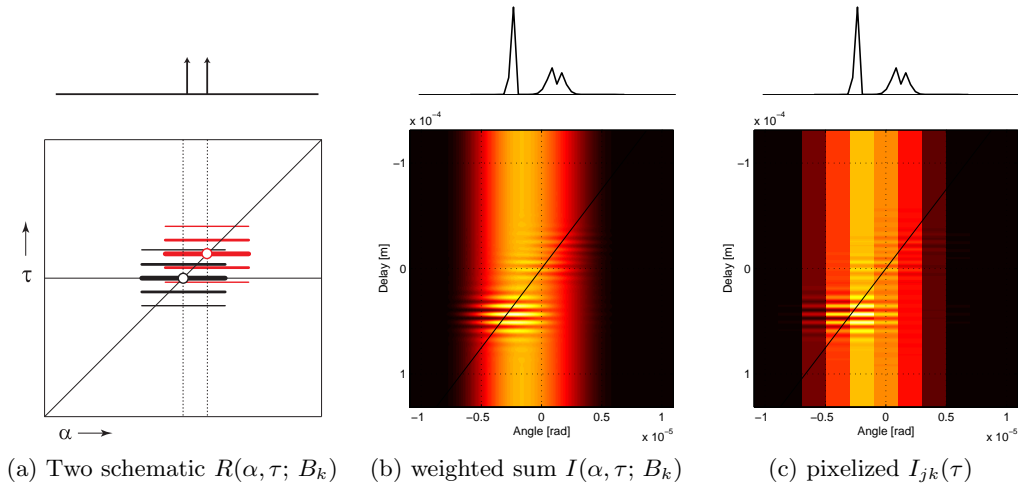


Figure 3. (a) Diagram of the detection space, for 2 point sources. Intensity patterns from the collection of point sources on the sky are summed. Per response function, the cross-section in one direction is an Airy profile. In the other direction, it is the polychromatic fringe pattern. The total – *baseline dependent* – response will be a sum of them, as depicted for an extended object in (b). The steepness of the diagonal is a function of baseline length since $\tau_B = B \sin \alpha \approx B\alpha$ and therefore the fringe contrast (as in narrow field interferometry) of the sum is baseline dependent. In (c) the pixelized example of the same extended scene is shown.

interference term (wavelength dependent weighting with w_λ^\dagger) can be implemented as a lookup-function in a polychromatic fringe packet. The summation (Eq. 1) is depicted for two point sources in Fig. 3a and for a continuous source in 3b,c.

The response on the detector is not measured continuously, but integrated on a few pixels with index $j = 1, 2, \dots, J$. Moreover, the summation in Eq. 1 is performed for every baseline setting with index $k = 1, 2, \dots, K$. As a result, the recorded intensities can be denoted as

$$I_{jk}(\tau) = \int_{\alpha_j - \frac{1}{2}\beta}^{\alpha_j + \frac{1}{2}\beta} I_k(\alpha, \tau) d\alpha, \quad (3)$$

where β is the angular width on the sky of one pixel.

The forward process described here can be seen as a multi-dimensional convolution (Eq. 2) and an integration (Eq. 3). These are two processes that will make that the inversion process – finding the luminosity function $L(\alpha)$ from recorded $I_{jk}(\tau)$ – is ill-posed. The solution of this inverse problem can only be estimated. We describe the inversion only briefly. If we denote the forward problem as

$$I_{jk}(\tau) = g[L(\alpha), B_k, \alpha_j], \quad (4)$$

then the inverse problem is

$$L(\alpha) = g^{-1}[I_{jk}(\tau)], \quad (5)$$

so that the sky distribution $L(\alpha)$ can be calculated given B_k and α_j , the lengths of the baselines at which the data were taken and the central locations of the pixels. In discrete form, this inverse problem is ill-conditioned since the response functions of neighboring point sources on the sky differ only slightly in α and τ . For estimates of the solutions, we apply routines by Hansen⁷ for Tikhonov regularization, based on singular value decomposition (SVD). To do so, the problem (Eq. 5) has to be written in the form

$$\begin{aligned} \mathbf{A} \cdot \mathbf{x} &= \mathbf{b} \\ \mathbf{x} &= \mathbf{A}_{\text{reg}}^{-1} \cdot \mathbf{b}. \end{aligned} \quad (6)$$

[†]The relative weights w_λ are chosen to be a Gaussian bandpass shape spanning the specified operation wavelengths.

Here, column vector $\mathbf{x} \simeq L(\alpha)$ is the function that we seek. The data is stored in column vector $\mathbf{b} \simeq [\dots; I_{jk}; \dots]$ so that all data (for all pixels as well as for all baselines) is stored as *measurement*. This means that operator \mathbf{A} performs the addition of response functions weighted by $L(\alpha)$ and the integration over the pixels.

3.2. Definition of forward and inverse problem — Homothetic

For this case, the convolution is rather straightforward. For every baseline length, there is one field-invariant convolution kernel that is only a function of α , not of τ . With the delay τ fixed, all point sources on the sky will produce a fringed intensity pattern on the detector. Complicated optics make this possible. The response functions (compare with Eq. 2) can now be expressed as

$$R(\alpha) = L(\alpha_0) \int_{k_{\min}}^{k_{\max}} \left| \frac{2J_1[\pi k D(\alpha - \alpha_0)]}{[\pi k D(\alpha - \alpha_0)]} \right|^2 w_\lambda [1 + \cos[\pi k B c(\alpha - \alpha_0)]] . \quad (7)$$

This function is only dependent on α_0 , the point-source location. Again, the response on the detector is not measured continuously, but integrated on many pixels. Since this number is large, the continuous coordinate α remains in use but is denoted as $\hat{\alpha}$:

$$I_k(\hat{\alpha}) = \int_{\alpha_j - \frac{1}{2}\beta}^{\alpha_j + \frac{1}{2}\beta} I_k(\alpha) d\alpha, \quad (8)$$

where β is the angular width on the sky of one pixel.

The calculation of the detector signals $I_{jk}(\tau)$ and $I_k(\hat{\alpha})$ for respectively the co-axial and the homothetic case is a straightforward summation of all response functions, weighted by the sky luminosity function $L(\alpha)$ (Eq. 1).

3.3. Shot Noise limited Detection

Recent developments in detector technology have led to CCDs for low light levels that can be assumed to provide shot noise limited read-out signals.¹⁵ We assume perfect quantum efficiency and no thermal or detector noise. To simulate shot noise limited interferometer responses, we assumed the theoretical intensities $I_{jk}(\tau)$ and $I_k(\hat{\alpha})$ to be temporal and spatial *probability distributions*.⁴ The photons will arrive with Poisson-distributed interval times and will be spatially distributed as well. The realization of the photon statistics is managed by the *Rejection Method*⁵ that will iteratively create a measurement vector with the theoretical intensity as distribution and Poisson statistics as input. For a very long integration time, an amount of 10^8 photons was assumed. The detected signals are displayed in Figs. 4 and 5. To give more detail on the bin-integration and quantization process, Fig. 6 was included as well. Here, the theoretical intensity is plotted over the ‘recorded’ photon counts (also expressed as intensity) for the co-axial case.

4. DISCUSSION AND COMPARISON

It should be noted that both sets of intensity data resemble each other a lot. Compared to the short period of the fringes, the signals can be assumed to be constant, even for the long-period-envelope in the Fizeau case. Hence, both of these signals represent a strong background signal with a small amplitude modulation on it. The difference is only that the modulation is either in τ - or α -direction. As a result, the expected performance for inversion will be quite the same. For low light levels, the number of available photons per pixel or per delay bin goes down and this limits the reconstruction.

The number of pixels for homothesis is related to the desired ultimate resolution. The number of bins for co-axial combination is *just as well* related to the ultimate resolution. In the first case, the spatial period of the fringes gets smaller for larger baselines and these fringes should remain resolvable. For the other case, the fringe period is a constant, but the central location of the fringe packet and the extent of it grow for larger baselines and hence more bins are needed to sample it.

Without a clever compensation scheme for the baseline length dependent external pathlength difference,²⁰ the ‘simple’ co-axial type will have a poor SNR for long baselines, just as the homothetic type. The homothetic type will have the same high number of bins (pixels) for the long as well as for the short baselines, whereas

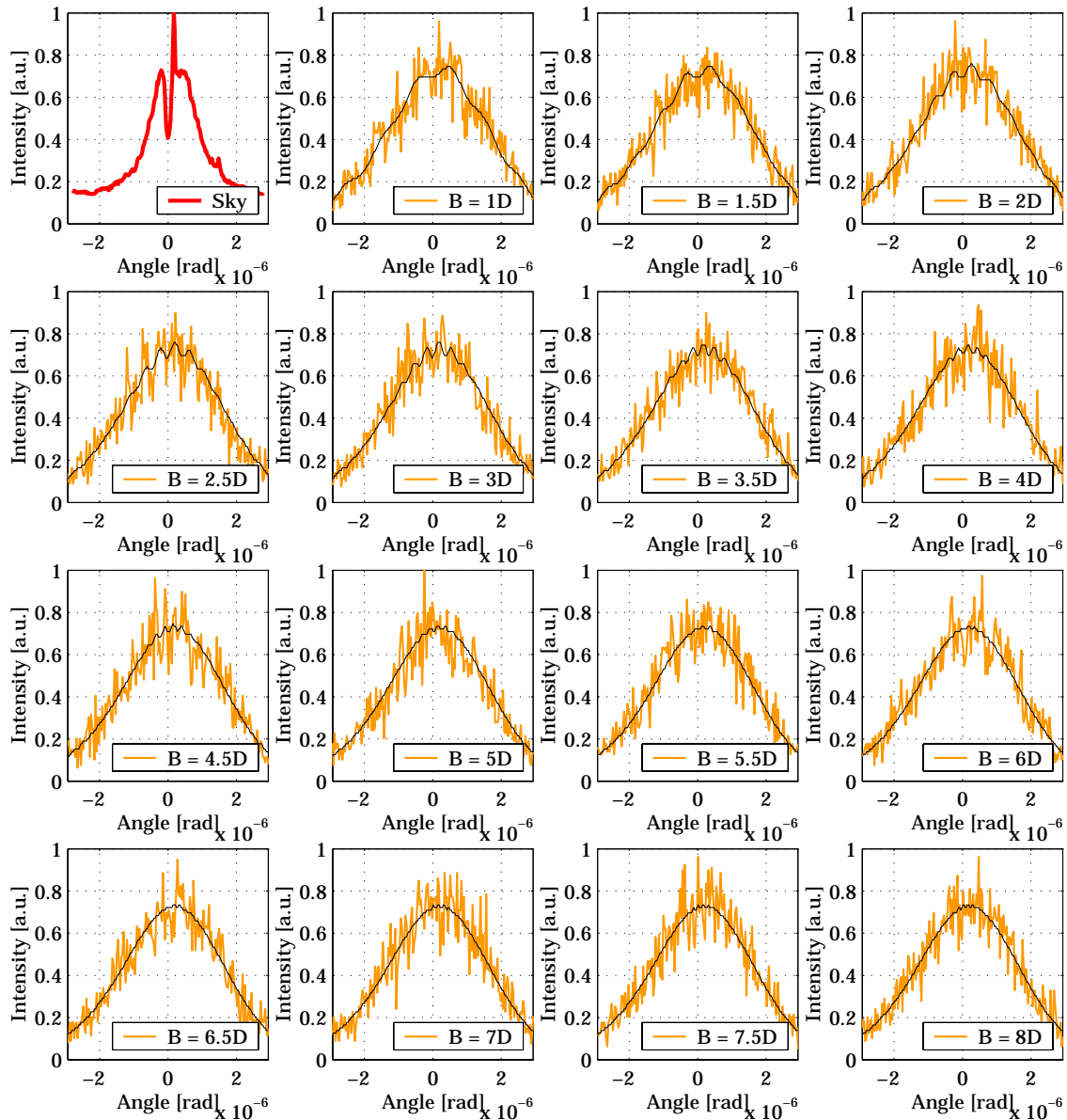


Figure 4. Tabular display of all **Fizeau** convolution results $I_k(\alpha)$, the recorded intensities (photon counts) per pixel for each baseline length. The number of pixels is 256. The baseline lengths are $B = D \cdot [1, \dots, 8]$ in steps of $D/2$. For these sketches, the number of photons was 10^5 , to illustrate the characteristics of the detector signals. The measurements are all normalized to one value, whereas the function on the sky is normalized to itself. The modulation amplitude as compared to the envelope is about 8% at best, since the source is partially resolved.

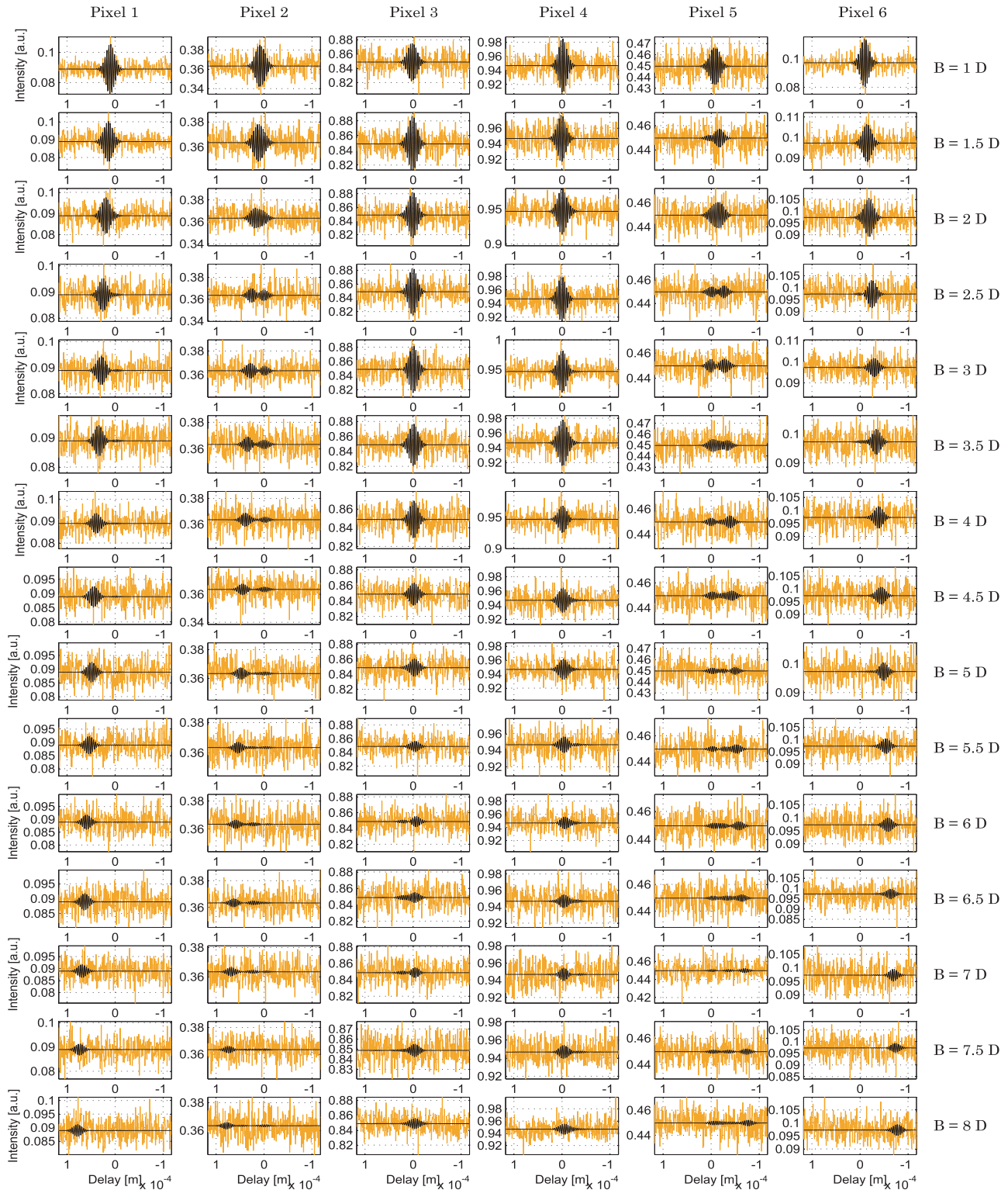


Figure 5. Tabular display of all Michelson $I_{jk}(\tau)$, the recorded intensities (photon counts) per pixel for each baseline length. The number of pixels is 6, the number of delay steps is 117. The baseline lengths are $B = D \cdot [1, \dots, 8]$ in steps of $D/2$. The fringes are sampled with 6 samples per λ_c and the total scan range ensures the ‘coverage’ of fringe packets for the longest baseline configuration on the outermost detectors. Observe the envelope widening and shifting for growing B .

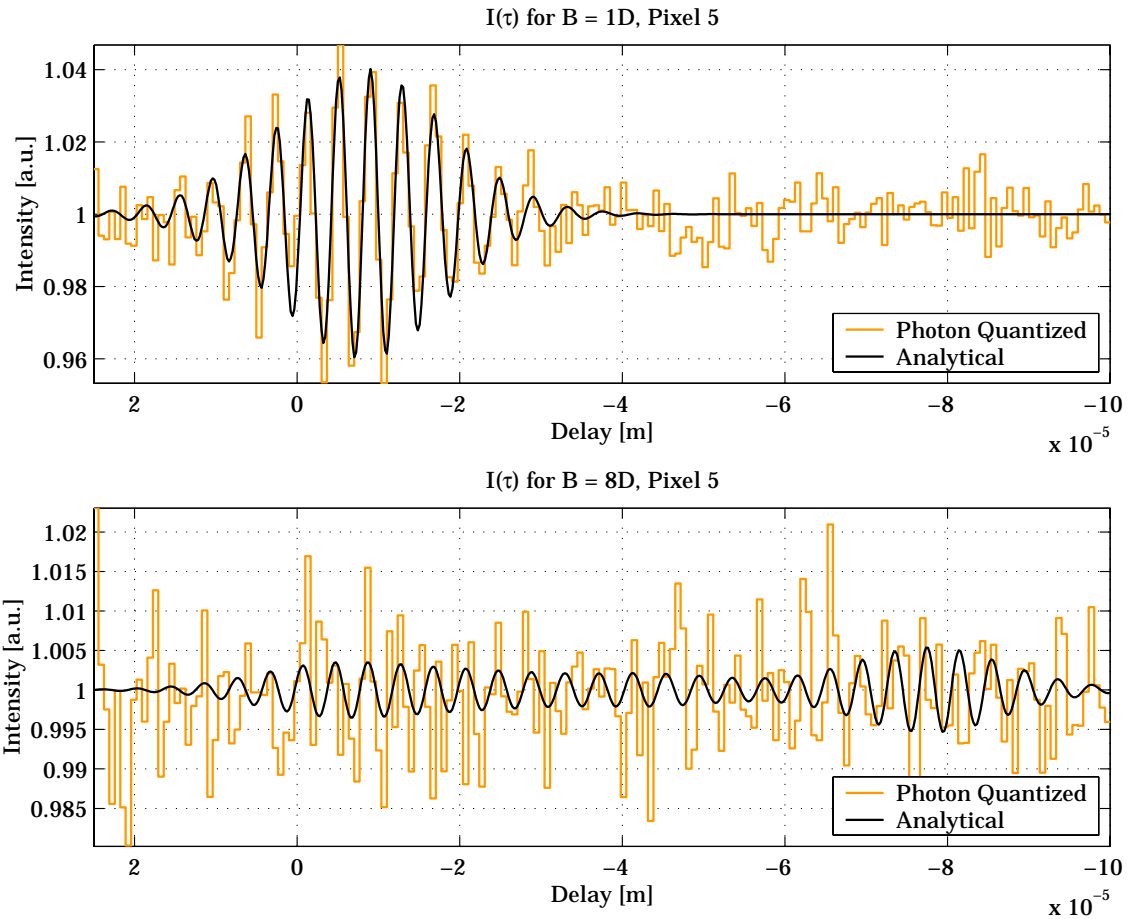


Figure 6. Detailed plot of two $I_{jk}(\tau)$, the recorded intensities (photon counts) per delay bin, for pixel $j = 5$ and baselines $k = 1, 15$, cf. Fig. 5. The period in each fringe packet is λ_c . Three effects appear very clearly from these plots. Firstly, the phase of the fringes with respect to the envelope change, which is in accordance with experiences from narrow field imaging. Secondly, the length of the fringe packet changes with baseline length. Finally, the shape of the envelope changes. To generate an image of the sky from these data, the three mentioned features must be included in the inversion process. A joint deconvolution of all collected intensity traces does just this. The modulation $1.04 - 0.96$ as compared to the average normalized signal 1 is again about 8% at best, as for the Fizeau case (Fig. 4).

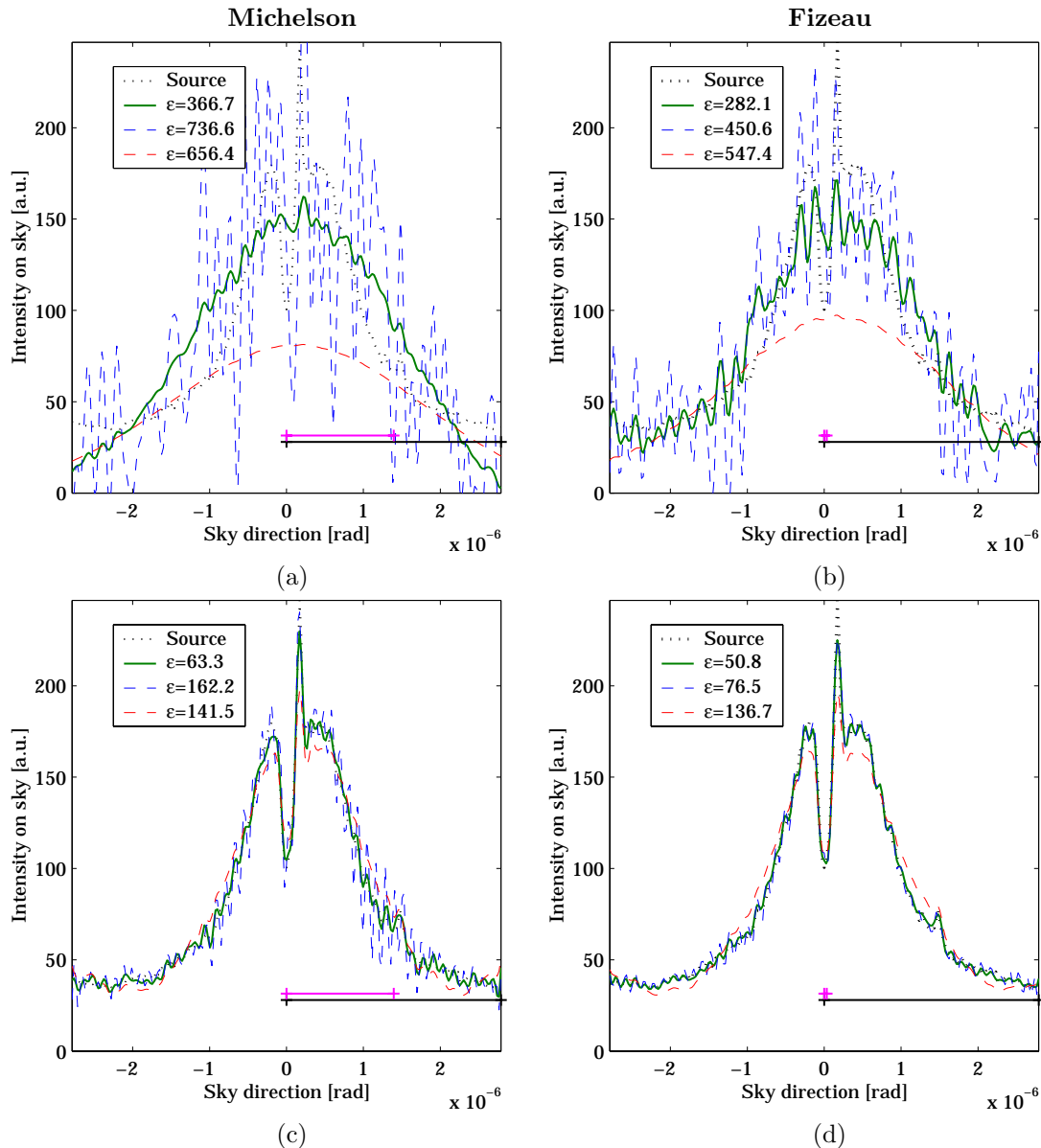


Figure 7. Top row: best blind reconstructions (continuous lines) of $L(\alpha)$ for the ‘Michelson’ and the ‘Fizeau’ cases when 10^5 photons in total were collected. The dashed lines indicate under- and over-regularized solutions (spikey and smooth). **Bottom row:** same as top row, but now for 10^8 photons available. The ϵ -values are the L^2 -norms of the differences with the now known original image; values below 231 indicate roughly a dynamic range of 1 : 100. Since the noise is different in every simulated detection–reconstruction run, the ϵ -values are not exactly equal to those displayed in Table 3. The horizontal lines in each plot indicate the detector pixel size and the diameter of the Airy disc, projected on the sky.

the co-axial type is allowed to have less bins for the shorter baselines. So for the photons per bin treatment of the SNR, the homothetic type has a constant value, whereas the co-axial type can have a decreasing value for growing baselines, but will end up in a SNR just as bad. The long baselines give the content of highest resolution in the sought image, but for both schemes, the SNR is low for long baselines. Treating the SNR as the amount of modulation on top of the background signal, both types display the same decrease of SNR for growing baselines. This effect is known as bandwidth smearing.

To compare the reconstruction possibilities at low light levels, the regularization routines (for blind imaging;

the source is unknown) are slightly assisted in finding the optimal filtering parameter. This is done to be able to present the best possible reconstruction. It should be noted however that the optimum found by the algorithms hardly differed from the tuned one. With the proper value for the regularization parameter Λ , a few reconstructions can be produced for $\bar{\Lambda} = \Lambda \cdot [1/5, 1, 5]$. In this way, the effects of over- and under-regularization can be seen, showing up as too spikey or too smooth solutions. For the reconstructions, the fit to the known object function can be given as a value ϵ . The L^2 -norm for a vector is used, given as

$$\epsilon = \sqrt{\sum_i |I_i - \hat{I}_i|^2}, \quad (9)$$

where ϵ is the fit error that we want to be low, and I_i and \hat{I}_i are the pixel intensity in the object function and the reconstruction, respectively. Some results are presented in Fig. 7.

The photon counts and reconstruction quality for decreasing light levels (shorter integration times or weaker sources) are listed in Table 3. Note that the number of resolution elements is 231, so an $\epsilon \simeq 231$ indicates a fit where all point intensities are recovered with an average error of 1, compared to the simulated average signal level of 100, which compares to a dynamic range of 1/100.

Table 3: Blind Imaging Performance

Photons	ϵ_{opt}		min., max.	
	Fizeau	Michelson	Photons/bin Fiz	Photons/bin Mich
10^8	42.6	71.7	1344, 59964	981, 13294
10^7	72.0	141.2	134, 5996	98, 1329
10^6	162.0	233.0	13, 600	10, 133
10^5	255.4	370.9	1, 60	1, 13

As predicted, the performance is nearly equal. The homothetic setup performs a bit better (reconstruction remains good down to 10^6 photons) but it should be noted that the co-axial type samples its fringes now with 6 bins per fringe period, which can be brought down to 4, thus limiting the number of bins and increasing the number of photons per bin.

The performance of the co-axial type could be greatly improved if the scanning range was reduced. A solution exists in the form of a Staircase Mirror. Simulations with the presented model on an interferometer with this addition are ongoing work. Another way to increase the performance is to limit the background presence relative to the modulated signal, since the fringes carry the high spatial frequency information. This could naturally be done by limiting the bandpass, but that will also limit the number of photons.

The homothetic setup performs well in this simulation, but the realization of the hardware needed to produce a scalable and reconfigurable array of entrance and exit pupils is complicated.¹² However, solutions exist¹⁹ for providing enough image and fringe stability to allow the assumption of a field-invariant convolution kernel. Should the kernel be field-variant in a known way, then imaging can still be performed, be it that the interferometric FOV is not as large as the single telescope FOV. The interferometric FOV can however be extended then by changing the delay, so that both spatial and temporal fringe encoding is used and interferometry can be done with only a few pixels and a few steps in delay. Also this method is being simulated and results will be published.

5. CONCLUSIONS

We have simulated the detector response for two imaging interferometers, imaging the same extended stellar object, with the same set of baseline configurations. Shot-noise limited detection was assumed. We have shown that both interferometers are capable of reconstructing the object and that they perform nearly equal for decreasing light levels. The simulated wide-field detector signals correspond to what is expected for both types and the calculation method allows the simulation of the response of hybrid or modified interferometer arrays, such as densified pupil imaging or imaging with the presence of a staircase-shaped mirror.

ACKNOWLEDGMENTS

The research described herein was performed mainly in the laboratories of TNO Science & Industry and Delft University of Technology. It was made possible by the *Space Research Organisation of the Netherlands* and was supported by the *Knowledge centre for Aperture Synthesis*, a collaboration of TNO Science & Industry, Delft University of Technology and Leiden Observatory. We would like to thank Rudolf LePoole for many fruitful discussions and critical remarks.

REFERENCES

1. A. Meinel, "Aperture synthesis using independent telescopes," *Applied Optics* **9**, pp. 2501–2504, 1970.
2. M. Shao and D.H. Staelin, 1977, "Long-baseline optical interferometer for astronomy," *J.Opt.Soc.Am.* **67**, 81.
3. M.A. Born and E. Wolf, 1980, *Principles of Optics*, Sixth edition, pp. 508 – 510.
4. J.W. Goodman, *Statistical Optics*, John Wiley & Sons, 1985.
5. W.H. Press, B.P. Flannery, S.A. Teukolsky and W.T. Vetterling, *Numerical Recipes in Pascal*, Cambridge University Press, 1989.
6. J.M. Beckers, "The VLTI, part III: Factors affecting wide field-of-view operation," *Advanced Technology Optical Telescopes IV, SPIE* **1236**, pp. 379–389, 1990.
7. P. C. Hansen, "Analysis of discrete ill-posed problems by means of the L-curve," *SIAM Rev.*, vol. **34**, no. 4, pp. 561580, Dec. 1992
8. T.J. Cornwell, 1994, "Wide field imaging III: mosaicing," *Synthesis Imaging in Radio Astronomy*, pp. 277 – 286.
9. D. Geman and C. Yong, "Nonlinear image recovery with half-quadratic regularization," *IEEE Trans. on Image Proc.*, Vol. **4**, No. 7, July 1995.
10. J.R.P. Angel, J.M. Hill, P.A. Strittmatter, P. Salinari and G. Weigelt, "Interferometry with the large binocular telescope," *Astronomical Interferometry, SPIE* **3350**, pp. 881–889, 1998.
11. J.G. Nagy and D.P. O'Leary, "Restoring images degraded by spatially variant blur," *SIAM J.Sci.Comput.* Vol. **19**, No. 4, pp. 1063–1082, July 1998.
12. L.A. d'Arcio, *Selected aspects of wide-field stellar interferometry*. PhD thesis, Delft University of Technology, November 1999.
13. M. Bertero and P. Boccacci, "Image restoration methods for the Large Binocular Telescope (LBT)," *Astron. & Astroph. Supplement Series* **147**, pp. 323 – 333, 2000.
14. *DARWIN The Infrared Space Interferometer Redbook*, ESA-SCI(2000) **12**, July 2000.
15. C.D. Mackay, R.N. Tubbs, R. Bell, D. Burt and I. Moody, "Sub-Electron Read Noise at MHz Pixel Rates," *SPIE* **4306**, pp. 289 – 298, January 2001.
16. G. Rousset, L.M. Mugnier, F. Cassaing and B. Sorrente, "Imaging with multi-aperture optical telescopes and an application," *C.R. Acad. Sci. Paris*, t. **2**, Série IV, pp. 17 – 25.
17. L.A. d'Arcio et al., 2002, "The imaging mode of the Infrared Space Interferometer IRSI-Darwin," *SPIE* **4838** 2002.
18. H. van Brug, T. van den Dool, W. Gieselen, P. Giesen, B. Oostdijck, and L. d'Arcio, "Delft testbed interferometer — Layout design and research goals," *Interferometry for Optical Astronomy II, SPIE* **4838**, pp. 425 – 429, August 2002.
19. C. van der Avoort, J.J.M. Braat et al., "Experimental Validation of Homothetic Mapping," *SPIE New Frontiers in Stellar Interferometry* **5491-185**, pp. 1587–1598, October 2004.
20. I. Montilla, S.F. Pereira and J.J.M. Braat, 2005, "Michelson wide-field stellar interferometry: principles and experimental verification," *Applied Optics*, vol. **44**, no. 3, pp. 328 – 336.